

Estimating the intrinsic dimension in fMRI space via dataset fractal analysis

Counting the ‘cpu cores’ of the human brain

Harris V. Georgiou (MSc, PhD)

Dept. of Informatics & Telecommunications,
National Kapodistrian Univ. of Athens (NKUA/UoA)

Email: harris@xgeorgio.info -- URL: <http://xgeorgio.info>

Abstract. Functional Magnetic Resonance Imaging (fMRI) is a powerful non-invasive tool for localizing and analyzing brain activity. This study focuses on one very important aspect of the functional properties of human brain, specifically the estimation of the level of *parallelism* when performing complex cognitive tasks. Using fMRI as the main modality, the human brain activity is investigated through a purely data-driven signal processing and dimensionality analysis approach. Specifically, the fMRI signal is treated as a multi-dimensional data space and its intrinsic ‘complexity’ is studied via *dataset fractal analysis* and *blind-source separation* (BSS) methods. One simulated and two real fMRI datasets are used in combination with Independent Component Analysis (ICA) and fractal analysis for estimating the intrinsic (true) dimensionality, in order to provide data-driven experimental evidence on the number of independent brain processes that run in parallel when visual or visuo-motor tasks are performed. Although this number is can not be defined as a strict threshold but rather as a continuous range, when a specific activation level is defined, a corresponding number of parallel processes or the casual equivalent of ‘cpu cores’ can be detected in normal human brain activity.

Keywords: fMRI, ICA, fractal dimension, fractal analysis, human brain

1 Introduction

Human brain is the most advanced and efficient signal-processing machine known today. It corresponds to only 2% of total body weight in adults (about 1.5 kg), yet it consumes 20% of blood oxygen and 25% of glucose, with only 20W at power peak. It consists of roughly 100 billion neurons with 1,000-10,000 synapse interconnections each, packed in 1130-1260 cm³ of volume, making it the most complex organ in the human body [42,14,30]. Analyzing its structure and functionality, especially during the actual process of some cognitive task or in relation to some mental impairment, has been a scientific challenge for centuries. However, only recent technological breakthroughs have enabled the study of the inner

1. INTRODUCTION

workings of living brains. Even today, simulating the structure and only basic neuron functionality of a full-scale human brain in a digital computer is still an infeasible task.

Functional Magnetic Resonance Imaging (fMRI) [33,30,45] is a powerful non-invasive tool for localizing and analyzing brain activity. Most commonly it is based on blood oxygenation level-dependent (BOLD) contrast, which translates to detecting localized changes in the hemodynamic flow of oxygenated blood in activated brain areas. This is achieved by exploiting the different magnetic properties of oxygen-saturated versus oxygen-desaturated hemoglobin.

In the human brain, tasks involving action, perception, cognition, etc., are performed via the simultaneous activation of a number of *functional brain networks* (FBN), which are engaged in proper interactions in order to effectively execute the task. Such networks are usually related to low-level brain functions and they are defined as a number of *segregated* specialized small brain regions, potentially distributed over the entire brain. In order to properly detect these activations and identify the set regions that constitutes a FBN related to a specific task, the 3-D space occupied by the brain is partitioned into a grid of ‘cubes’ or *voxels*. Each voxel constitutes the elementary spatial unit that acts as a signal generator, recorded and registered as a low-resolution 1-D time series. Actual fMRI voxel signals from brain scans can be considered as a mixture of various components or *sources* with different temporal and spatial characteristics. These sources can be classified as of interest and as artifacts [7].

In order to understand the true functionality and full potential of the human brain, data-intensive approaches are required for analyzing the actual brain signal (e.g. fMRI, EEG) during specific cognitive tasks. Current research involves multi-disciplinary endeavors, from Biochemistry and Neurophysiology to Simulation and VLSI design, with projects like the Human Brain Project (HBP) by EU [18] and Brain Research through Advancing Innovative Neurotechnologies (BRAIN) by USA [47]. There is also very active research and development effort in the industry, where projects like the recently announced ‘TrueNorth’ chip by IBM implement a million-scale neural network grid in special-purpose VLSI and extremely high power efficiency [37,44]. However, all these efforts are currently focused on the *structural* properties of the human brain, i.e., the neural networks topology and connectivity, while the *functional* and higher-level cognitive properties are still very difficult to model. In practice, this means that the hardware necessary to build and fully simulate (at the neuron cell level) an actual artificial ‘brain’ equivalent to a small animal’s now becomes available, but the problem of turning this construction to a machine with actual cognitive and abstract functionality still remains (for the most part) unsolved, with only application-specific modules being developed successfully (e.g. artificial retina implants, with some visual processing capabilities [15]).

This study focuses on one very important aspect of the functional properties of human brain, specifically the estimation of the level of *parallelism* when performing complex cognitive tasks. In some very abstract sense, this is not much different than trying to recover the (minimum) number of actual ‘cpu cores’

required to ‘run’ all the active cognitive tasks that are registered in the entire 3-D brain volume while performing a typical fMRI experimental protocol that includes visual-only or visuo-motor tasks.

Using fMRI as the main modality, the human brain activity is investigated through a purely data-driven signal processing and dimensionality analysis approach. Specifically, the fMRI signal is treated as a multi-dimensional data space and its intrinsic complexity is studied via *dataset fractal analysis* and *blind-source separation* methods. Section 2.1 provides an overview of the fMRI experiments and the nature of sensory data; section 2.2 defines a proper mathematical formulation for the *data unmixing* task and its importance in understanding the true sources of brain activity; section 3.1 provides hints to proper data dimensionality reduction in fMRI; section 3.2 briefly describes the basic methodology for dataset fractal analysis and how it is applied for the estimation of the *intrinsic dimensionality* of the fMRI data space; section 3.3 briefly describes ICA as a typical approach for blind-source separation in signal processing; sections 4.1, 4.2 and 4.2 describe the simulated and real fMRI datasets used in this study; section 5 includes the experiments and results, using all the methods and datasets described earlier; sections 6 and 7 conclude the study with discussion of the results and their practical meaning.

2 Problem Definition

2.1 The nature of fMRI data

In experimental fMRI procedures, there are two common activation schemes: the *block* paradigms and the *event-related* paradigms [5]. In the block paradigm, the subject is presented with a specific stimulus for a specific time frame, e.g., a set of images of different placement, colors, patterns or categories, and the subject has to press a switch to signal positive or negative feedback as a response. In the event-related paradigm, the subject is exposed to a series of randomized short-time inputs, e.g., a noise or a pain stimulus, with or without the need for specific response from the subject. In both cases, the external input is considered as a primary ‘source’ and is temporally correlated with the brain activity. Areas of high activation and correlation to the stimulation/response pattern are considered as highly relevant to the specific functional task (visual/motor centers, pain receptors, etc). The same procedure can be followed when there is no specific external paradigm, constituting the *steady-state* functional analysis of brain activity. In this setup, there is no correlation to previously known activation pattern and hence the analysis is essentially a search for functionally independent sources in the recorded fMRI signal.

The acquired fMRI signal is registered in both spatial (3-D) and temporal (1-D) domain, resulting in a composite 4-D signal. Each spatial axis is registered as a grid of spatial resolution 3-5 mm³, resulting in a 3-D grid of voxels. Typically, a complete volume of voxel data, e.g. 60x60x30 to 64x64x48, is recorded every 1-2 seconds for a sequence of 100-150 time points [33,30,45]. This produces a total of roughly 108K-197K voxels for every time frame or, equivalently, 11e6

2. PROBLEM DEFINITION

to 30e6 data points organized as a two-dimensional matrix, where each row corresponds to a complete brain ‘snapshot’. In practice, the number of actual brain voxels is smaller, since non-brain areas of the grid are masked out before any further processing; however, the data volume still remains within the same order of magnitude. Additionally, typical fMRI experimental protocols involve several subjects, in order to exclude any subject-specific characteristics that may affect the statistical properties of the fMRI data under consideration. Clearly, this creates a high-volume data analysis process that makes it a very complex and computationally demanding task.

In terms of signal processing, the hemodynamic response function (HRF) [33,30,45] of the activated neurons, i.e., the changes in oxygen-rich blood flow in the time domain, acts as a low-pass filter in the temporal domain, which in turn modifies the true activation signal that it is registered as fMRI data. In other words, the HRF of the activated neurons, i.e., the changes in oxygen-rich blood flow in the time domain, modifies the true activation time-series signal that it is registered for each brain voxel as fMRI data. Moreover, the HRF is known to be spatially-varying, which means that there are slightly different hemodynamic responses for different areas of the brain, as well as different HRFs between different subjects. This means that traditional regression approaches like General Linear Model (GLM) approximations [33,45,30] that require a pre-defined ‘design matrix’ are clearly sub-optimal, since it is typically constructed as permutations, transformations, time-shifts and derivatives of one (assumed) ‘universal’ HRF. There are also additional features that makes this approximation even more difficult in practice, such as the fact that the voxels’ activations are assumed to be statistically independent (while locally they are not, due to the physical properties of the veins and hemodynamics), as well the various artifacts that are introduced to the signal by external factors (scanner drift, electronic noise, head movements, respiration, cardiac pulsation, etc) [33,30,45].

2.2 Understanding brain activity

In fMRI analysis, the sources of interest include task-related, transiently task-related and function-related sources, meaning that in a task-specific fMRI experiment most of the task-related activity is expected to be spatially isolated and temporally synchronized with the corresponding input/stimulation patterns. Therefore, these sources are expected to appear as super-Gaussian in nature due to the spatial and temporal localization of such task-related brain functionality.

Special matrix factorization algorithms are required to reformulate the fMRI data as a multiplication of two other matrices, where one is for the time courses of the estimated signal ‘sources’ and one for the corresponding spatial maps of related brain activity. Formally put, if $\mathbf{Y} \in \mathbb{R}^{t \times n}$ is the full fMRI data matrix with t rows as time points and n brain voxels ‘unwrapped’ into a linear vector, then the fMRI data matrix can be factorized as $\mathbf{Y} = \mathbf{T}\mathbf{S}$, $\mathbf{T} \in \mathbb{R}^{t \times p}$, $\mathbf{S} \in \mathbb{R}^{p \times n}$, where the p spatial maps are collected as rows in \mathbf{S} and each column of \mathbf{T} contains the activation pattern along time for the corresponding spatial map.

In GLM [33,45,30], \mathbf{T} is the pre-defined ‘design matrix’ that contains permutations, transformations, time-shifts and derivatives of one (assumed) ‘universal’ HRF, while \mathbf{S} is the matrix of the corresponding regressor coefficients in each row. Although the GLM approach is sufficient when only specific sensory-related signal sources (external stimuli) are considered, in the general case it is not possible to define a global design matrix for all signal sources and all (multiple) subjects. Instead, Independent Component Analysis (ICA) is the most commonly used method for this task, in the context of blind source separation (BSS) [25,8,27] (see section 3.3).

While GLM and ICA are the dominating approaches for directed or blind unmixing models, respectively, in fMRI analysis, the large volume of voxel data and the inherent properties of the fMRI signals make the unmixing task highly demanding in both memory and computational resources. Moreover, proper identification of ‘universal’ FBNs requires multiple experiments with different subjects, which means working with multiplied volume of sensory data or combining multiple unmixing results over various runs [17,10]. In either case, unmixing algorithms are required to be both fast and accurate in identifying the signal ‘sources’ of fMRI data and the activated areas in the brain corresponding to the specific paradigm source.

Based on these properties, it is clear that the analysis of fMRI data, in the sense of its decomposition into distinct sources and the identification of the ones related to a specific task or functional activity in the brain, is a very difficult task. The lack of strict specifications for a ‘universal’ HRF and background artifacts, hence in turn for an accurate pre-defined ‘design matrix’ for a standard GLM model, makes it a typical candidate for BSS approaches such as ICA, as well as alternative approaches like Dictionary Learning (DL) and Compressive Sensing (CS). Recently, there is an increased interest for alternatives to ICA for data-driven fMRI unmixing. Notably good results have been attained with Dictionary Learning (DL) - based fMRI analysis [32,2,3]. Also, an improved variation of K-SVD was proposed as the basis for Dictionary Learning (DL), customized to fMRI analysis [29].

3 Dimensionality analysis of the fMRI data space

3.1 Data decimation and intrinsic dimensionality

One way to deal with the high complexity of the BSS task in fMRI data is to reduce the number of voxels under consideration. Specifically, adjacent neurons in the brain can be considered highly correlated in terms of their responses to external stimuli, provided that the blood vessel networks at very small scales actually introduce some spatio-temporal correlation. Hence, their BOLD response and HRF can be considered, at some degree, statistically dependent. If the spatial resolution of the fMRI signal is high, adjacent voxels in the original 2-D or 3-D volume scan can be considered statistically redundant. Therefore, some form of decimated voxels set can be used instead as input for the unmixing task,

3. DIMENSIONALITY ANALYSIS OF THE fMRI DATA SPACE

without sacrificing the accuracy of identifying the true inherent sources of the data.

In fMRI, using decimated versions of the original data in the spatial and/or the temporal domain is not an uncommon practice. Indeed, some works refer to sub-sampling the fMRI in a spatial (voxels) or temporal (time points) sense, when the resolution is considered high enough. However, this has been applied only as a one-time pre-processing step in the preparation of data, i.e., before any real BSS analysis is conducted (e.g. see in [31,32]). Furthermore, the decimation ratio used in each case is chosen in a purely empirical way, since there are currently no analytical studies with regard to the resulting quality of the decimated fMRI data.

Spatio-temporal correlations between voxels and statistical dependencies are essentially the reason why the fMRI data space has an intrinsic (true) dimensionality much smaller than the number of voxels, i.e., the data matrix $\mathbf{Y} \in \mathbb{R}^{t \times n}$ is of column rank $c \ll n$. However, for proper unmixing of the fMRI data, the column rank of matrix \mathbf{Y} should be retained even when some decimation process is employed. In other words, the selection of a smaller subset of voxels (instead of all) should be conducted in a way that does not destroy the information content of the full data, but instead exploit the fact that the number of voxels n is very large and their inherent statistical properties can be properly retained with a much smaller subset.

In the cases when only a small set of the signal sources are considered, i.e., the time series of some external stimuli (plus some transformations of it), then regression methods like GLM can be easily formulated with the proper ‘design matrix’ to recover the related brain activity. When the analysis is conducted in the BSS sense, i.e., all major signal sources are to be recovered (including the stimuli time series), then decomposition methods like ICA provide a well-formulated statistical framework for this task, as long as the proper constraints are asserted as valid (most importantly, the assertion of at most one Gaussian signal source). However, when these statistical assertions are not fully satisfied or when there is a large number of signal sources that are ‘exponentially decaying’ in terms of importance (contribution to the mixed signal’s variance, power spectrum and approximation error), then the number of independent components that ICA or other similar algorithms is limited only by some external pre-defined threshold. In other words, the data matrix $\mathbf{Y} \in \mathbb{R}^{t \times n}$ can be factorized *approximately* as $\mathbf{Y} \simeq \mathbf{TS}$, $\mathbf{T} \in \mathbb{R}^{t \times p}$, $\mathbf{S} \in \mathbb{R}^{p \times n}$, with the reconstruction error becoming smaller as p increases. In theory, if the true sources of the mixed signal are perfectly separable in the BSS sense, then ICA will stop after recovering exactly $p = c$ components, where $c \ll n$ is the column rank of the data matrix \mathbf{Y} . This means that there are exactly p components, i.e. time courses and corresponding activation maps, that can fully reconstruct the fMRI data for the entire brain activity. Hence, the definition of the optimal value for p by means of non-parametric (data-driven) estimation procedure is of utmost importance in the BSS task for fMRI unmixing.

3.2 Dataset fractal analysis

In recent years, dimensionality analysis in signal processing has been extensively linked to fractal analysis and *fractal dimension*, as a non-parametric method for the quantitative characterization of the complexity or ‘randomness’ of a signal [16,34]. When applied to 1-D signals, metrics like the *Hurst exponent* or *Lyapunov exponent* have been used as statistical features to describe various types of data series, from biomedical signals (e.g. EEG, ECG, etc) to financial and climate time series. In 2-D signals, these methods provide additional features for characterizing the texture of images, e.g. when analyzing biomedical modalities (radiology, ultrasound, MRI, etc) [9]. Fractal dimension is closely linked to these fractal parameters and it provides a clear distinction between the *embedding* space, i.e., the full-rank space in the algebraic sense, from the actual space spanned by the registered sensory data. In the general case when fractal analysis is applied to some multi-dimensional signal, the estimation of the fractal dimension can be used as a realistic evaluation of the ‘complexity’ of the space spanned by the actual data points available and, hence, a very useful hint regarding the inherent redundancy in a given dataset.

In order to establish a preliminary estimation of the complexity and intrinsic dimensionality of datasets, fractal analysis provides a data-centric approach for this task. Dataset fractal analysis, specifically the calculation of *intrinsic fractal dimension* (FD) of a dataset, provides the quantitative means of investigating the non-linearity and the correlation between the available ‘features’ (i.e., dimensions) by means of dimensionality of the embedding space [9,39]. Fractal dimension has also been used as an alternative way of characterizing the discriminative power of each ‘feature’ separately, thus providing a non-statistical way of ranking them in terms of importance, e.g. as means of non-parametric feature selection in classification tasks [46]. The fractal analysis of datasets has been used successfully in previous studies [35,19,36] and it has been proven very valuable as a tool for comparing arbitrary datasets of extracted features with the qualitative clinical properties that an experience physician uses to characterize a mammographic image.

The two most commonly used methods of calculating the fractal dimension of a dataset are the *pair-count* (*PC*) and the *box-counting* (*BC*) algorithms [34,39,43,16]. In the pair-count algorithm, all Euclidean distances between the samples of the dataset are calculated and a closure measure is then used to cluster the resulting distances space into groups, according to various ranges r , i.e., the maximum allowable distance within samples of the same group. The *PC* value is calculated for various sizes of r and it has been proved that $PC(r)$ can be approximated by:

$$PC(r) = K \cdot r^D \quad (1)$$

where K is a constant and D is called pair-count exponent. The $PC(r)$ plot is then a plot of: $\log(PC(r))$ versus $\log(1/r)$, i.e., D is the slope of the linear part of the $PC(r)$ plot over a specific range of distances r . The exponent D is called *correlation fractal dimension* of the dataset, or D_2 .

3. DIMENSIONALITY ANALYSIS OF THE FMRI DATA SPACE

The box-counting approach calculates the exponent D in a slightly different way, in order to accommodate case of large datasets with size in the order of thousands; however, it essentially calculates an approximation of that same correlation fractal dimension value, i.e., D_2 . It is commonly used when the datasets contain large number of samples, usually in the order of thousands [46,4]. In this case, instead of calculating all distances between the samples, the input space is partitioned into a grid of n -dimensional cells of side equal to r . Then, the samples inside each cell are calculated and the frequency of occurrence R_r , i.e., the count of samples in a cell, divided by the total number of samples, is used to approximate the correlation fractal dimension by:

$$D_2 = \frac{\partial \log \sum_i (R_r^i)^2}{\partial \log (1/r)} \quad (2)$$

Ideally, both pair-count algorithm and box-counting algorithm calculate the same value, i.e., the correlation fractal dimension D_2 of the initial dataset, which characterizes the intrinsic (true) dimension of the input space [4]. In other words, D_2 would be the *minimum dimension of the dataset* if only ‘perfect’ features were allowed, i.e., totally uncorrelated and with the best discriminative power available within the specific set of features.

In this study, fractal feature analysis was applied to both the initial set of qualitative characteristics, provided by the expert physician, as well as the constructed datasets of morphological features. In all cases, the pair-count algorithm employing Euclidean distances was used, due to the relatively small number of samples available, as well as the better stability and accuracy for D_2 against the box-counting approach [43].

In order to calculate the slope at the linear part of the $PC(r)$ plot, a parametric sigmoid function was used for fitting between the sample points of the plot. In the parametric sigmoid function:

$$y = y_0 + C_y \left(\frac{1}{1 + \exp(-C_x(x - x_0))} \right) \quad (3)$$

the (x_0, y_0) identifies the transposition of the axes, while C_x and C_y identify the appropriate scaling factors. Specifically, the value of C_x affects the steepness of the central part of the curve, while C_y specifies the Y -axis width of the sigmoid curve. Then, the slope of the linear part around the central curvature point, i.e. the value of D_2 , is:

$$\frac{\partial^2 y(x_0)}{\partial x^2} = 0 \Rightarrow D_2 = \frac{\partial y(x_0)}{\partial x} = \frac{C_x \cdot C_y}{4} \quad (4)$$

The fitness of the parametric sigmoid over a range of samples assumes uniform error weighting over the entire range of data. Thus, if a large percentage of points lies near the upper bound ($y = y_{max}$) or lower bound ($y = y_{min}$) of the Y -axis range, as in most cases of $PC(r)$ plots, then the fitness in the central region of the sigmoid, i.e., where the slope is calculated, can be fairly poor. For

this reason, an additional weighting factor was introduced in the fitness calculation in this study. Specifically, the Tukey (tapered cosine) parametric window function [21] was applied over the Y -axis range when calculating the overall fitness error of the sigmoid. The Tukey window is parametric (q -value) in terms of the exact form around its center, ranging from completely rectangular ($q = 0$) to completely triangular or Hanning window ($q = 1$). When applied over the Y -axis range, the rectangular case is equivalent to calculating the fitness error uniformly over the entire range, while the triangular case is equivalent to calculating the fitness error primarily against the central point of the sigmoid curve. In this study, all fitness calculations employed Tukey windows as error weighting factors, using parameters q in the range between 0.5 and 1.0 for optimal slope results. The equation for computing the coefficients w_j of a discrete Tukey window of length N ($j = 1 \dots N$) is as follows:

$$w_j = \begin{cases} \frac{1}{2} \left(1 + \cos \left(\frac{2\pi(j-1)}{q(N-1)} - \pi \right) \right) & , \quad 1 \leq j < \frac{q}{2} (N-1) \\ 1 & , \quad \frac{q}{2} (N-1) \leq j \leq N - \frac{q}{2} (N-1) \\ \frac{1}{2} \left(1 + \cos \left(\frac{2\pi}{q} - \frac{2\pi(j-1)}{q(N-1)} - \pi \right) \right) & , \quad N - \frac{q}{2} (N-1) < j \leq N \end{cases} \quad (5)$$

3.3 Independent Component Analysis (ICA)

In blind source separation (BSS), ICA has been successfully applied to fMRI data for many years [25,8,27,13]. Since the fMRI consists of a mixture of unknown components, corresponding to different brain sources of activity, the unmixing procedure is essentially a BSS problem. However, due to the relatively low temporal and spatial resolution of fMRI data, the non-stationary properties of the signal due to brain- and machine-state variations, as well as the unknown number and exact statistical properties of the sources, the BSS of fMRI data is not a trivial task.

ICA is based on identifying non-Gaussian properties between the sources and separating them from the mixture, essentially reconstructing the original signal as a linear combination of identified components, i.e., similarly to the previously discussed formulation $\mathbf{Y} = \mathbf{T}\mathbf{S}$, $\mathbf{T} \in \mathbb{R}^{t \times p}$, $\mathbf{S} \in \mathbb{R}^{p \times n}$. In this case, \mathbf{S} is the matrix of independent components (spatial maps of brain activity) and \mathbf{T} is the mixture matrix (corresponding time courses). In fMRI, the ICA can be performed in the spatial or temporal dimension of the (vectorized) voxel data, producing either spatial or temporal components in matrix \mathbf{S} . Several studies have been conducted in whether spatial or temporal ICA works better for BSS in fMRI data [8]; however spatial maps, i.e., retrieving \mathbf{S} as spatial components, seem to be more accurate and useful in most clinical applications of fMRI. The two most common approaches for ICA are the Infomax [6] and fastICA [26,24,25] algorithms.

Although ICA has been widely studied and employed in fMRI, recent works have identified the relevant advantages of analyzing brain activity under the

4. DATASETS

sparsity, instead of statistical independency, of the underlying mixture of individual components. Additionally, the BSS problem itself has been identified by few researchers as equivalent to Dictionary Learning (DL) [1,2,32,31,29], which is already used in various applications.

Since ICA does not include any sparsity constraints (like in DL), while at the same time it assumes specific statistical properties for the underlying signal sources (at most one Gaussian distribution, minimal noise artifacts). Hence, ICA unmixing of fMRI data that do not fully satisfy these constraints will construct factorizations that include the maximum allowable number of components for the reconstruction of the original (mixed) data with the minimum error. In other words, as described in section 3.1, when the fMRI data include non-trivial mixtures of sources (as in the case of the simulated dataset, see section 4.1), ICA will construct a factorization model $\mathbf{Y} \simeq \mathbf{T}\mathbf{S}$, $\mathbf{T} \in \mathbb{R}^{t \times p}$, $\mathbf{S} \in \mathbb{R}^{p \times n}$, with $p = p_{max}$ and non-zero reconstruction error. Similar problems emerge when using sparsity-aware approaches as in DL [29], since they typically produce factorizations with $p \ll p_{max}$ (here, p_{max} is the dictionary size), but with larger reconstruction errors, as expected.

In this study, ICA is used as one of the most popular approaches in BSS problems like the fMRI unmixing task. In the simulated fMRI datasets (see section 4.1), ICA provides an exact estimation of the intrinsic dimensionality of the signal, which is expected to be lower than the pre-defined sources used in the mixture. In the real fMRI datasets (see sections 4.2 and 4.2), ICA provides approximate factorization models and a quantitative way to track the signal reconstruction error as the number of used components changes. In both cases, the factorization models provided by ICA are used as a verification tool for validating the quality of the estimated fractal dimension of each dataset. Although the exact numbers between p_{max} and the fractal dimension calculated differ due to their inherently different meaning, tracking their changes in parallel and comparing results is used here as a valuable tool for dimensionality analysis of the fMRI datasets.

4 Datasets

The investigation of fMRI space complexity and intrinsic dimensionality was conducted with two separate types datasets, namely one of simulated fMRI data and two of real fMRI data from carefully designed experiments. The simulated data were introduced as the means to verify the recoverability of the intrinsic dimension when the real signal sources are known and well-defined, while the real data were used as guidelines for estimating the true brain activity in two typical cognitive tasks (visual recognition task and visuo-motor task).

4.1 Simulated fMRI datasets

In this study, an adapted version of the real-valued fMRI data generator code from the MSLP-Lab [38] toolbox was used for creating artificial fMRI data as a

mixture of eight main sources [13]. Using the basic knowledge of the underlying statistical characteristics of the underlying sources, the components include three highly super-Gaussian sources (S1, S2, S5), a Gaussian source (S4) and a sub-Gaussian source (S3), plus two more super-Gaussian sources (S6, S8) and a sub-Gaussian source (S7). The time course for each component defines the temporal characteristics of the corresponding source, namely one task-related (S1), two transiently task-related (S2, S6) and several artifact types (S3, S4, S5, S7, S8), including respiration, cardiac pulsation, scanner drift, background noise, etc. These sources can be considered as spatial maps that are activated according to their time course and mixed linearly to produce the final (simulated) fMRI data.

Although in typical fMRI experiments there is only one sensory ‘input’ (stimulation), here the full set of eight sources (S1...S8) was considered throughout the evaluation. Specifically, the simulated fMRI data included eight spatial maps of size 60x60 voxels (2-D ‘slices’) and a 100-point time course, with statistical properties as described above. Each spatial map was linearized by row-concatenation into a (row) vector of 3600 voxels, registered along its time course (column) vector of 100 points. Finally, these eight 100x3600 matrices of spatio-temporal maps were mixed linearly to produce the final eight-source mixing of simulated fMRI data into one matrix of that same size. Hence, in terms of the problem formulation presented in section 2.2, the final matrix of (simulated) fMRI data is registered as $\mathbf{Y} \in \mathbb{R}^{t \times n}$, where $t = 100$ time points and $n = 60^2 = 3600$ voxels. Since the final data matrices are always linearized in a similar way before applying any unmixing algorithm, using 2-D ‘slices’ of (simulated) voxels instead of full 3-D (real) brain scans in each time point affects only the volume of the data and not the task itself.

4.2 Real fMRI datasets

ds101 – The ‘Simon’ task The ‘NYU Simon Task’ dataset [28] comprises of data collected from 21 healthy adults while they performed a rapid event-related Simon task. On each trial, the inter-trial interval (ITI) was 2.5 seconds, with null events for jitter), a red or green box appeared on the right or left side of the screen. Participants used their left index finger to respond to the presentation of a green box, and their right index finger to respond to the presentation of a red box. In congruent trials the green box appeared on the left or the red box on the right, while in more demanding incongruent trials the green box appeared on the right and the red on the left. Subjects performed two blocks, each containing 48 congruent and 48 incongruent trials, presented in a pre-determined order (as per OptSeq), interspersed with 24 null trials (fixation only).

Functional imaging data were acquired using a research dedicated Siemens Allegra 3.0 T scanner, with a standard Siemens head coil, located at the NYU Center for Brain Imaging. The data obtained were 151 contiguous echo planar imaging (EPI) whole-brain functional volumes (TR=2000 ms; TE=30 ms; flip angle=80, 40 slices, matrix=64x64; FOV=192 mm; acquisition voxel size=3x3x4 mm³) during each of the two Simon task blocks. A high-resolution T1-weighted anatomical image was also acquired using a magnetization prepared gradient

4. DATASETS

echo sequence (MPRAGE, TR=2500 ms; TE= 3.93 ms; TI=900 ms; flip angle=8; 176 slices, FOV=256 mm).

The ‘ds101’ dataset is hosted by Openfmri.org for public access in raw NiFTI format [40], including voxel masks and brain map template, but without any pre-processing (head movement, sensor drift, etc).

In this study, the data from nine (out of 21) subjects were used, including two runs each, for a total of 18 datasets of fMRI scans. Each dataset was masked for exclusion of non-brain areas and thresholded for exclusion of brain areas with near-zero activity. The resulting number of voxels ranged roughly between 28K and 39K, while the number of snapshots was fixed to 151 time points. In terms of the formulation of section 2.2, each fMRI data matrix is $\mathbf{Y} \in \mathbb{R}^{t \times n}$ with $t = 151$ time points and $27631 \leq n \leq 38735$ ‘non-zero’ voxels.

Three variants of each dataset were used, regarding the smoothing pre-filtering. Specifically, according to standard fMRI acquisition practice, a Gaussian smoothing kernel was applied to the original 3-D voxel space, in order to suppress noise artifacts and enhance the spatial continuity of the voxel data. With respect to their *Full Width at Half Maximum* (FWHM) [11,12], or $2\sqrt{2 \cdot \ln 2} \cdot \sigma \simeq 2.35482 \cdot \sigma$ for Gaussian kernels, two different spatial sizes were used: 4 mm^3 and 8 mm^3 . In practice, since the voxel resolution in this dataset is $3 \times 3 \times 4 \text{ mm}^3$, the smaller kernel performs (softer) averaging on 1-1.33 neighboring voxels, while the larger kernel performs (more aggressive) averaging on 2-2.67 neighboring voxels. These two ‘smoothed’ versions, plus the original non-smoothed version, are the three variants of each dataset, used throughout the experiments (see section 5 for details).

ds105 – Visual object recognition task The ‘Visual Object Recognition Task’ dataset [22,20,23,41] comprises of data collected from six healthy adults while they performed a visual recognition task. Neural responses, as reflected in hemodynamic changes, were measured in six subjects (five female and one male) with gradient echo echoplanar imaging (EPI) on a GE 3T scanner (General Electric, Milwaukee, WI) (repetition time (TR) = 2500 ms, 40 3.5-mm-thick sagittal images, field of view (FOV) = 24 cm, echo time (TE) = 30 ms, flip angle = 90), while they performed a one-back repetition detection task. High-resolution T1-weighted spoiled gradient recall (SPGR) images were obtained for each subject to provide detailed anatomy (124 1.2-mm-thick sagittal images, FOV = 24 cm).

Stimuli were gray-scale images of faces, houses, cats, bottles, scissors, shoes, chairs, and nonsense patterns. The categories were chosen so that all stimuli from a given category would have the same base level name. The specific categories were selected to allow comparison with our previous studies (faces, houses, chairs, animals, and tools) or ongoing studies (shoes and bottles). Control nonsense patterns were phase-scrambled images of the intact objects. Twelve time series were obtained in each subject. Each time series began and ended with 12 s of rest and contained eight stimulus blocks of 24-s duration, one for each category, separated by 12-s intervals of rest. Stimuli were presented for 500 ms with an

interstimulus interval of 1500 ms. Repetitions of meaningful stimuli were pictures of the same face or object photographed from different angles. Stimuli for each meaningful category were four images each of 12 different exemplars.

The ‘ds105’ dataset is hosted by Openfmri.org for public access in raw NiFTI format [40], including voxel masks and brain map template, but without any pre-processing (head movement, sensor drift, etc).

In this study, the data from six (all) subjects were used, including three (out of 12) runs each, for a total of 18 datasets of fMRI scans. Each dataset was masked for exclusion of non-brain areas and thresholded for exclusion of brain areas with near-zero activity. The resulting number of voxels ranged roughly between 22K and 47K, while the number of snapshots was fixed to 121 time points. In terms of the formulation of section 2.2, each fMRI data matrix is $\mathbf{Y} \in \mathbb{R}^{t \times n}$ with $t = 121$ time points and $22387 \leq n < 47192$ ‘non-zero’ voxels.

Three variants of each dataset were used, regarding the smoothing pre-filtering. Specifically, according to standard fMRI acquisition practice, a Gaussian smoothing kernel was applied to the original 3-D voxel space, in order to suppress noise artifacts and enhance the spatial continuity of the voxel data. With respect to their *Full Width at Half Maximum* (FWHM) [11,12], or $2\sqrt{2} \cdot \ln 2 \cdot \sigma \simeq 2.35482 \cdot \sigma$ for Gaussian kernels, two different spatial sizes were used: 4 mm^3 and 8 mm^3 . In practice, since the voxel resolution in this dataset is $3 \times 3 \times 3.5 \text{ mm}^3$, the smaller kernel performs (softer) averaging on 1.14-1.33 neighboring voxels, while the larger kernel performs (more aggressive) averaging on 2.29-2.67 neighboring voxels. These two ‘smoothed’ versions, plus the original non-smoothed version, are the three variants of each dataset, used throughout the experiments (see section 5 for details).

5 Experiments and Results

Two separate sets of experiments were conducted in this study, one for BSS unmixing via ICA and one for dataset fractal dimension estimation. Both sets included all three fMRI datasets, namely one of simulated fMRI data and two of real fMRI data experiments (see sections 4.1, 4.2, 4.2).

5.1 ICA analysis of the datasets

The ICA experiments that were conducted with the simulated fMRI data included two distinct realizations of the dataset, generated by the same procedure and the same specifications as described in section 4.1. Since the data generation includes several noise components, the two realizations were used as an additional verification check to validate that slightly different mixtures of (artificial) fMRI data do not produce significant differences in the ICA error-versus-components plots and estimated dataset fractal dimension.

Figure 1 presents the time courses of the ICA factorization (matrix \mathbf{T}), with the blue curves representing each of the eight ideal (true) sources and the red curves representing the corresponding ICA-recovered sources. Figure 2 illustrates

5. EXPERIMENTS AND RESULTS

the corresponding activation maps (matrix \mathbf{S}) recovered by ICA, spatially reshaped into proper 2-D brain ‘slices’, where the reconstruction errors are visible as artifacts (‘ghost’ artifacts).

Fig. 1. Ideal (blue) and ICA-recovered (red) time courses of the eight sources in the simulated fMRI dataset. Parameter r is the correlation coefficient between the original (ideal) and the recovered time course, p is the corresponding p-value and $rmse$ is the matching error. The first component (upper-left corner) corresponds to the pre-defined external stimuli.

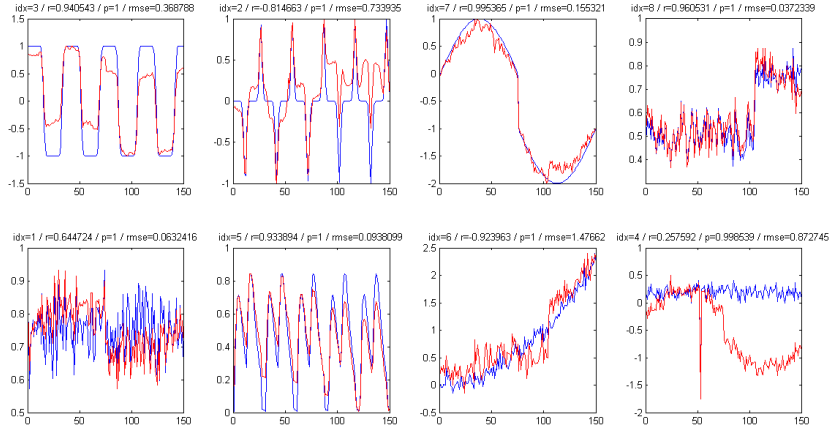


Figure 3 presents the plot of reconstruction error (RMSE) versus the number of ICA components used. Specifically, after the ICA unmixing model is complete, the ICA components are used one by one in rank-1 reconstructions of the original data and the corresponding errors are used for sorting the components in ascending order (smallest RMSE first). Subsequently, a set of components starts from the first one (top of the list) and increased by adding the next one in each step, while estimating and registering the corresponding reconstruction error. The plot illustrates the total reconstruction error decreasing almost linearly as the number of used components increases, as expected. It should be noted that for ‘perfect’ ICA factorizations, as in the case of simulated fMRI data, the number of components recovered by ICA is exactly the same as the number of signal sources (true) used in the mixture that created these data (see section 4.1).

The ICA experiments that were conducted with the real fMRI data included two distinct datasets, ‘ds101’ and ‘ds105’, as described in sections 4.2 and 4.2, respectively. Instead of a single 2-D brain ‘slice’ as in the case of the simulated fMRI data, here the datasets employ full 4-D fMRI data, i.e., 3-D voxel grid of the brain volume evolving in 1-D time course. Figure 4 illustrates a real example of a 2-D brain ‘slice’ for a single time point, as it is registered in the ‘ds101’ dataset; the data are in raw unprocessed mode and no background-exclusion masking.

Fig. 2. ICA-recovered activation maps of the eight sources in the simulated fMRI dataset, spatially reshaped into proper 2-D brain ‘slices’. The lower-left box corresponds to the activation areas for the pre-defined external stimuli. The lower-right box illustrates the complete reconstructed fMRI mixture at time point $t = 150$.

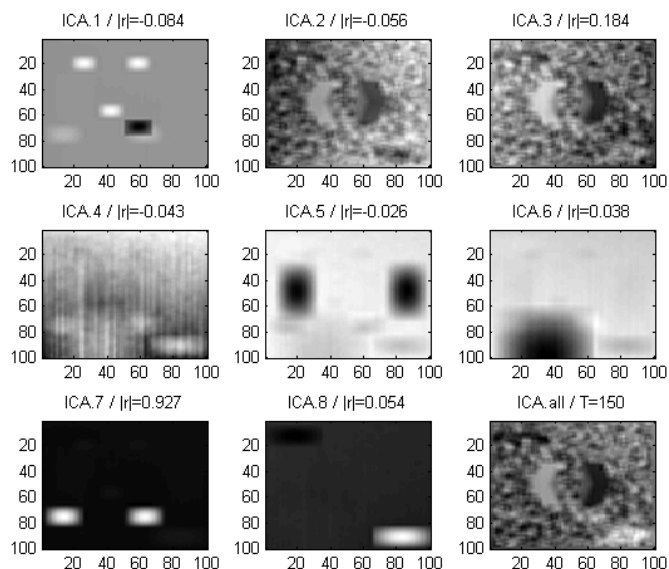
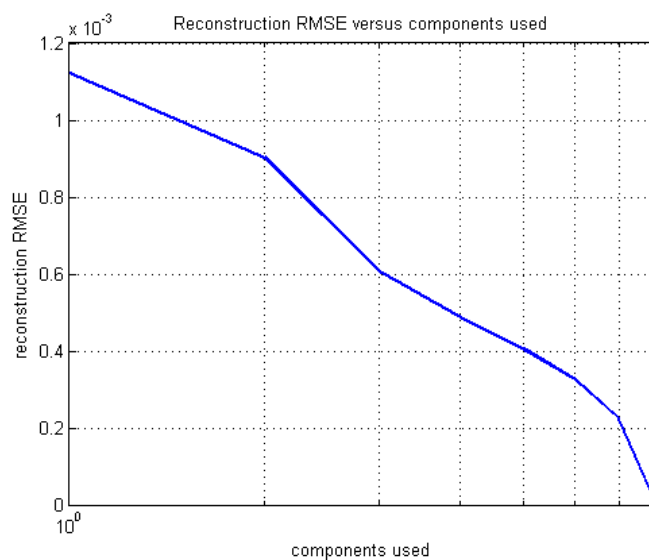


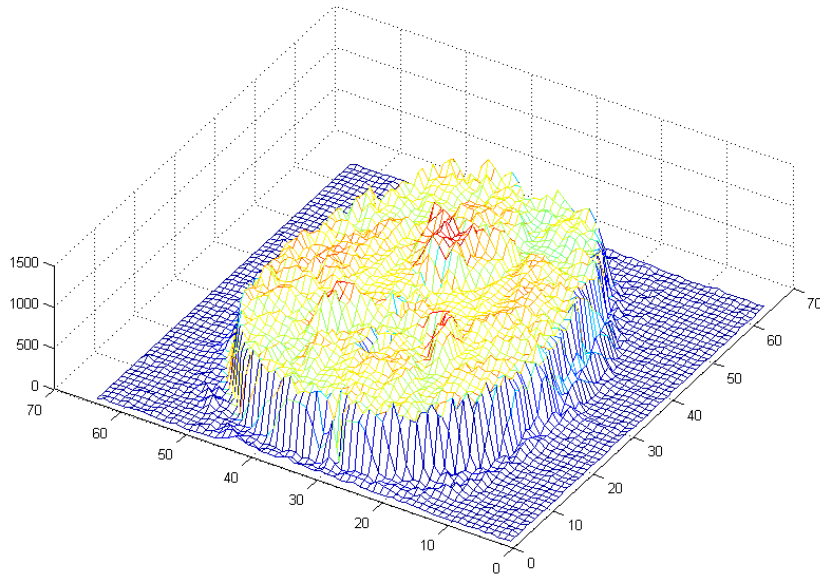
Fig. 3. Reconstruction error versus number of used components. ICA detects exactly eight components, i.e., the number of true signal sources in the original mixture, and the final reconstruction error is practically zero.



5. EXPERIMENTS AND RESULTS

Signal-independent noise is evident in the flat/blue areas, i.e., are outside the brain volume.

Fig. 4. Real example of a 2-D brain ‘slice’ for a single time point, as it is registered in the ‘ds101’ dataset (unprocessed, no background-exclusion masking).

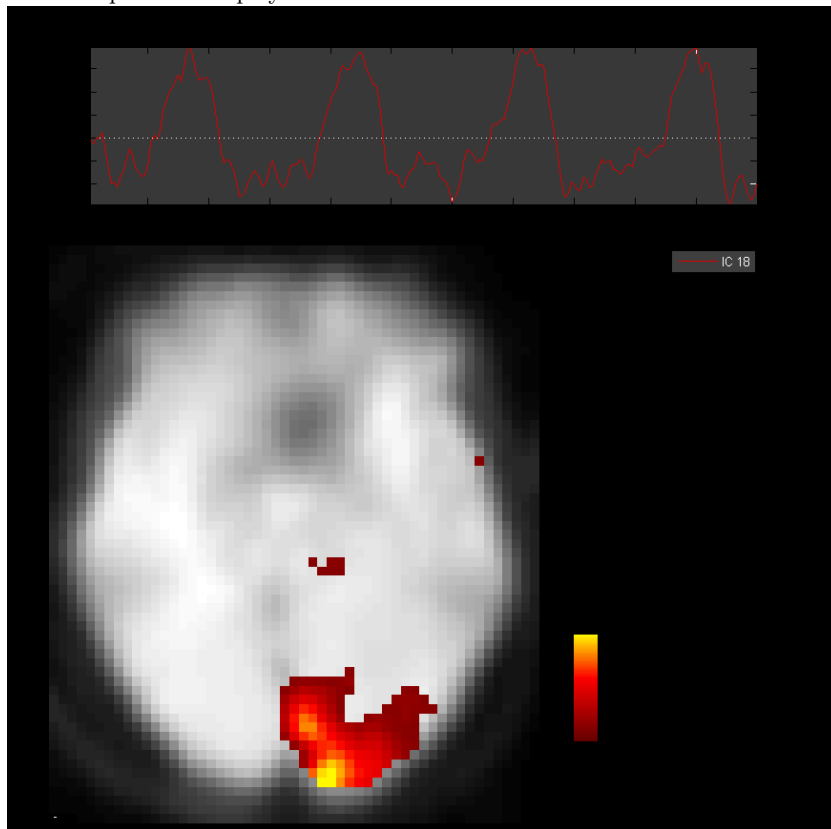


Using the GIFT toolbox for Matlab [13], Figure 5 illustrates the ICA-recovered time course (red plot) and the corresponding 2-D ‘flattened’ activation map that represents the actual response of the human brain in a visuo-motor task very similar to the experimental protocol employed in the ‘ds101’ dataset. Here, the ICA successfully recovered one particular component very similar to the external stimuli, which ideally is a square-shaped pulse modulated by the HRF (see section 2.1), instead of the noisy sinusoid curve.

Figure 6 illustrates 10 of the 50 ICA-recovered time courses of components in a sample run with the ‘ds101’ dataset. Although the ICA converged successfully with the minimum attainable reconstruction error, the unmixing model failed to detect one single component that closely matches the ideal time course of the stimuli. However, it is evident that one component (third from top-left) matches component no.7 and two components (upper/lower left) match component no.8 of the simulated fMRI data as illustrated in Figure 1 in terms of overall shape and noise characteristics.

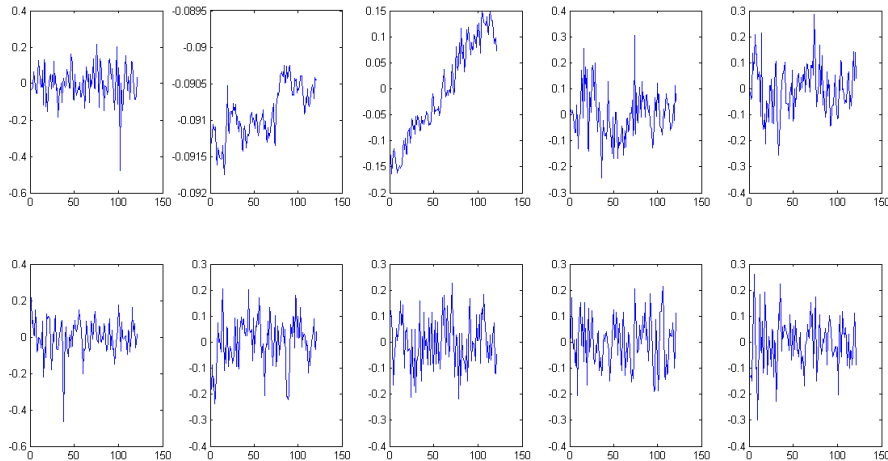
With respect to reconstruction error versus number of used components, Figure 7 and Figure 8 illustrate how the RMSE changes (drops) as the size of the ICA mixture becomes larger. Red curves represent the RMSE against the number of used components up to an upper limit of 10, 25, 50 and 100. The final

Fig. 5. Sample result from the GIFT toolbox for Matlab [13], illustrating the ICA-recovered time course (red plot) and the corresponding 2-D ‘flattened’ activation map of the actual response of the human brain in a visuo-motor task very similar to the experimental protocol employed in the ‘ds101’ dataset.



5. EXPERIMENTS AND RESULTS

Fig. 6. ‘ds101’ (non-smoothed), 10 of the 50 ICA-recovered time courses of components in a sample run.



(right-most) point in blue represents the maximum-size, lowest-RMSE in each case. Hence, the general slope of the red curves, as well as the dotted blue line connecting the end points, illustrate the robustness of the ICA unmixing process in each of the real fMRI dataset.

5.2 Dataset fractal analysis and intrinsic dimensionality

Similarly to the ICA experiments, the dataset fractal analysis that was conducted with the simulated fMRI data included two distinct realizations of the dataset, generated by the same procedure and the same specifications as described in section 4.1. Since the data generation includes several noise components, the two realizations were used as an additional verification check to validate that slightly different mixtures of (artificial) fMRI data do not produce significant differences in the estimation of the fractal dimension of the dataset.

Figure 9 presents the log-log plot for the box-counting method of estimating the fractal dimension (FD) in the simulated fMRI dataset, as described in section 3.2. Specifically, the blue points represent instances of $\log(PC(r))$ versus $\log(1/r)$, and the blue curve is the best-fit parametric sigmoid that is described by Eq.3. The FD is recovered as the slope of the curve in the central point at (x_0, y_0) , according to Eq.4.

Based on the box-counting approach described in section 3.2, the two realizations of the simulated fMRI data resulted in FD values of 3.774 and 3.884, using the complete dataset with no decimation (100 sample vectors). This means that an average mean value of 3.83 can be considered as a reliable estimate of the fractal dimension of the dataset.

Fig. 7. ‘ds101’ (non-smoothed), ICA reconstruction error versus number of used components. Red curves represent the RMSE against the number of used components up to an upper limit of 10, 25, 50 and 100. The final (right-most) point in blue represents the maximum-size, lowest-RMSE in each case.

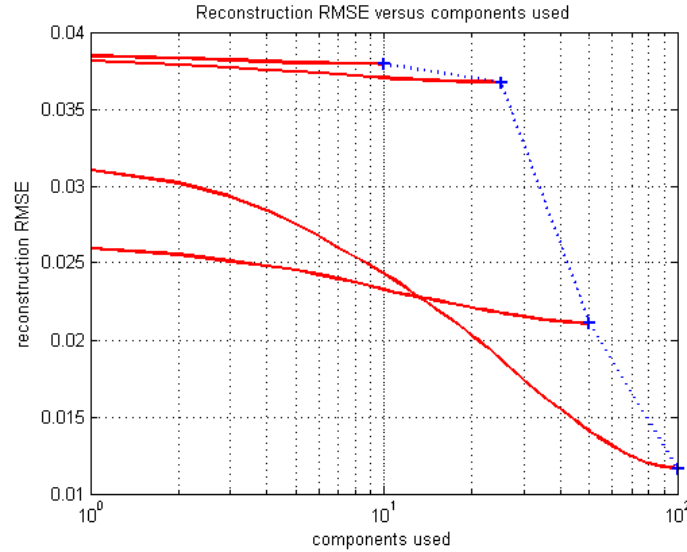
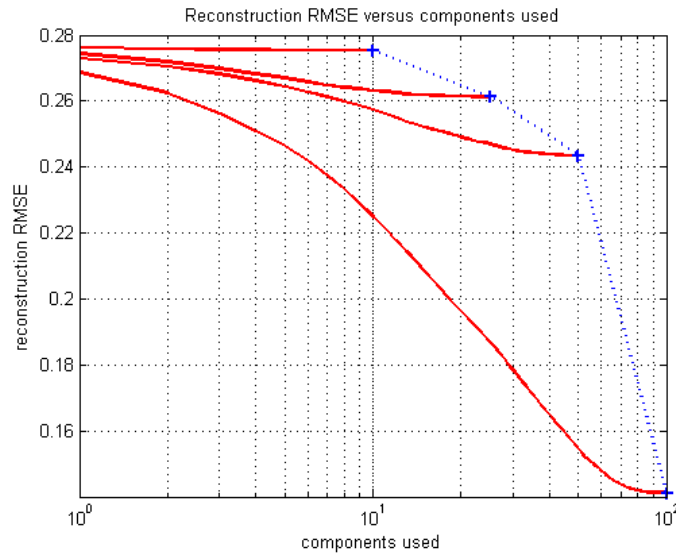
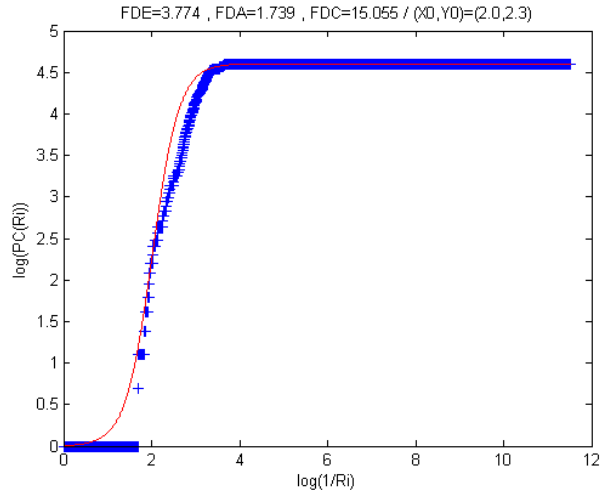


Fig. 8. ‘ds105’ (non-smoothed), ICA reconstruction error versus number of used components. Red curves represent the RMSE against the number of used components up to an upper limit of 10, 25, 50 and 100. The final (rightmost) point in blue represents the maximum-size, lowest-RMSE in each case.



5. EXPERIMENTS AND RESULTS

Fig. 9. The log-log plot $\log(PC(r))$ versus $\log(1/r)$ (blue points) and the best-fit parametric sigmoid (red curve) that recovers the fractal dimension (‘FDE’) of the simulated fMRI dataset.



The dataset fractal analysis experiments that were conducted with the real fMRI data included two distinct datasets, ‘ds101’ and ‘ds105’, as described in sections 4.2 and 4.2, respectively. Instead of a single 2-D brain ‘slice’ as in the case of the simulated fMRI data, here the datasets employ full 4-D fMRI data, i.e., 3-D voxel grid of the brain volume evolving in 1-D time course.

Figure 10 presents the log-log plot for the box-counting method of estimating the fractal dimension (FD) in the ‘ds105’ dataset, as described in section 4.2; the corresponding plot for ‘ds101’ is similar (omitted). Specifically, the blue points represent instances of $\log(PC(r))$ versus $\log(1/r)$, and the blue curve is the best-fit parametric sigmoid that is described by Eq.3. The FD is recovered as the slope of the curve in the central point at (x_0, y_0) , according to Eq.4.

Based on the box-counting approach described in section 3.2, the ‘ds101’ and ‘ds105’ datasets were analyzed for multiple subjects and various choices of smoothing kernel size (see sections 4.2 and 4.2, respectively, for details). Table 1 presents the FD estimations for the ‘ds101’ dataset; Table 2 presents the FD estimations for the ‘ds105’ dataset. The results include the mean values and the corresponding confidence range at the significance level $\alpha = 0.05$, as well as the standard deviations. Plain values correspond to trimmed sets excluding the smallest and largest value, while values in parentheses correspond to the non-trimmed (complete) sets. In both tables, each cell corresponds to FD estimation in 18 instances (9x2 for ‘ds101’ and 6x3 for ‘ds105’).

Fig. 10. The log-log plot $\log(PC(r))$ versus $\log(1/r)$ (blue points) and the best-fit parametric sigmoid (red curve) that recovers the fractal dimension ('FDE') of the 'ds105' dataset (smoothed, $sm=8mm^3$).

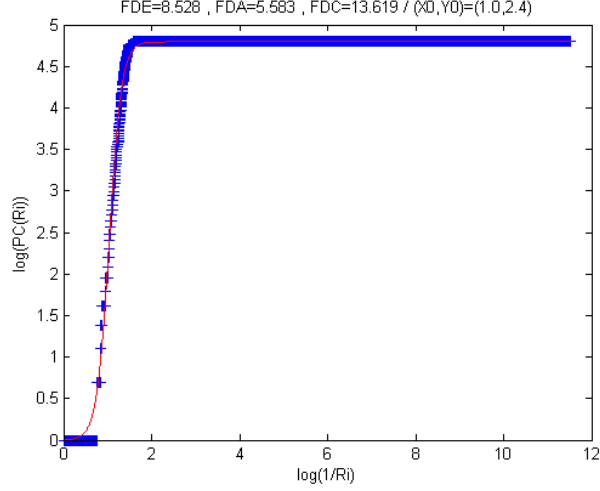


Table 1. FD estimation in the 'ds101' dataset for various smoothing kernel (sm) sizes. Plain values correspond to trimmed sets excluding the smallest and largest value, while values in parentheses correspond to the non-trimmed (complete) sets. Each cell corresponds to FD estimation in 18 instances (9×2). Confidence range for mean value is at the significance level $\alpha = 0.05$.

	mean (μ)	conf.range ($\mu \pm$)	stdev (σ)
(no sm)	61.07 (60.43)	11.73 (12.57)	23.93 (27.20)
$sm=4mm^3$	31.92 (31.59)	5.13 (5.62)	10.48 (12.17)
$sm=8mm^3$	11.27 (17.14)	2.15 (2.49)	4.39 (5.38)

Table 2. FD estimation in the 'ds105' dataset for various smoothing kernel (sm) sizes. Plain values correspond to trimmed sets excluding the smallest and largest value, while values in parentheses correspond to the non-trimmed (complete) sets. Each cell corresponds to FD estimation in 18 instances (6×3). Confidence range for mean value is at the significance level $\alpha = 0.05$.

	mean (μ)	conf.range ($\mu \pm$)	stdev (σ)
(no sm)	15.38 (17.38)	2.86 (5.56)	5.83 (12.04)
$sm=4mm^3$	12.79 (13.75)	2.20 (3.31)	4.48 (7.16)
$sm=8mm^3$	10.67 (11.01)	1.59 (1.89)	3.24 (4.09)

6 Discussion

The results presented in section 5.2, as well as the ICA unmixing models that were presented in section 5.1, verify that there is indeed a limited number of activated brain areas during standard cognitive processes. Since these activations are present simultaneously, they provide a hint of how many tasks are ‘running’ in the human brain *in parallel* as part of its every day functionality.

In section 5.1, the results from experiments with simulated fMRI data illustrate the basic unmixing problem for brain sensory data, which is relevant not only to fMRI but other modalities too, e.g. in EEG. The results show that ICA can indeed address the unmixing task with moderate to good performance, especially with regard to the signal sources related to well-defined external stimuli (see component no.7 in Figure 1 and Figure 2). Due to the nature of ICA and its inherent constraints, not all signal sources can be correctly identified and, hence, the recovered components do not match the original ones perfectly; however, if the statistical assertions about the signal sources are satisfied adequately, the total reconstruction error can be minimized effectively. For the simulated fMRI dataset, the total RMSE for the ICA mixture, reconstructing the original signal with all the recovered (eight) components, is practically zero (see Figure 3). The most important results in this case are: (a) the number of ICA components recovered matches the number of true sources used to construct the original mixture and (b) one of the recovered components closely matches (highly correlated) with the well-defined external stimuli (square-shaped time course). This is extremely important in real fMRI experimental protocols, where specific stimuli types are to be correlated to specific brain areas for constructing ‘global’ brain *atlases*.

The ICA experiments with the real fMRI datasets ‘ds101’ and ‘ds105’, described in section 5.1, illustrate the true performance of ICA in constructing factorizations for real brain data. Here, the data volume is much larger than in the case of simulated data, since the voxel grid is now 3-D instead of a single 2-D ‘slice’, while at the same time the inherent statistics are much more complex, as expected. From Figure 5 and Figure 6 it is clear that ICA works as expected, providing ‘dense’ (non-sparse) unmixing models with satisfactory performance; however, it is not always clear what is the nature of each of the recovered components and how they can be interpreted, especially when specific signal sources are in question other than a pre-defined external stimuli (e.g. scanner drift, electronic noise, head movements, respiration, cardiac pulsation, etc).

As described in sections 3.3 and 3.1, in the case of real fMRI datasets the ICA factorization is only approximate (RMSE is never zero) and the minimum reconstruction error is achieved only when using the maximum allowable number of components - which, in turn, is ICA-limited by the number of time points available (i.e., t in matrix $\mathbf{Y} \in \mathbb{R}^{t \times n}$). In other words, a ‘perfect’ unmixing model in real brain data requires the largest possible number of components to be retrieved. On the other hand, from Figure 7 and Figure 8 it is clear that the reconstruction error drops sharply when the number of used components is

much lower than this upper limit. For the ‘ds101’ dataset, this number seems to be somewhere in $25 < p < 50$ (see Figure 7), while for the ‘ds105’ dataset it is $p \simeq 50$ (see Figure 8). In both cases, the non-smoothed variants of the datasets were used, hence there is no loss of fine-detail activations and these estimations can be considered as realistic and consistent.

With regard to the fractal analysis on the simulated fMRI data, results in section 5.2 illustrate the robustness and consistency of this method. Figure 9 presents the log-log plot used to estimate the FD in this case, i.e., the intrinsic dimension of the dataset, which is calculated as $3.83 (\pm 1.45\%)$. This value is consistent with the results of other studies using the same dataset with sparsity-aware realizations of factorization models [29], where the estimated sparsity is clearly lower (6 or less) than the number of signal sources used in the original mixture. Furthermore, Figure 9 shows the robustness of the method, with the use of a parametric sigmoid function and Tukey window, even when the log-log plot does not provide a clear hint for the selection of the linear part from where the slope should be extracted.

For the real fMRI datasets, Tables 1 and 2 present the detailed estimations of the FD for smoothed and non-smoothed variants. Specifically, Table 1 shows the mean FD values for the ‘ds101’ dataset, including the confidence range and the standard deviation. It is clear that, even in the non-smoothed ‘noisy’ variant, the intrinsic dimension of the space spanned by the voxel data is much lower ($48 < D < 63$) than the dimension of the embedding space ($27K < n < 39K$). Furthermore, the value of FD becomes smaller, as expected, when smoothing is applied to the data prior to the fractal analysis process. This proves that the method is consistent in terms of following the decreasing ‘complexity’ of the dataset, as well as the fact that smoothing the fMRI voxel data can enhance the quality of the most important information content (major brain activity areas), with a possible loss in fine details and/or low-level activations. Hence, smoothing options in fMRI should be carefully selected in relation to the specifications of each task, i.e., sensitivity versus specificity requirements.

Similar comments are valid for the ‘ds105’, according to the results in Table 2. In the non-smoothed ‘noisy’ variant, the intrinsic dimension of the space spanned by the voxel data is, again, much lower ($12 < D < 19$) than the dimension of the embedding space ($22K < n < 48K$) and it becomes even smaller, as expected, when smoothing is applied to the data prior to the fractal analysis process. Figure 10 shows the log-log plot used to calculate the FD value for the smoothed variant ($sm=8mm^3$) of the dataset, where it is clear that the proposed fractal analysis method provides a very reliable estimation. Furthermore, it shows a much better fit in the sigmoid curve, which means that the box-counting method (see section 3.2) becomes more reliable, as expected, when the fMRI data are smoothed.

As it was mentioned earlier, this study focuses on the estimation of the level of *parallelism* when the human brain is performing complex cognitive tasks. In some very abstract sense, this is not much different than trying to recover the (minimum) number of actual ‘cpu cores’ required to ‘run’ all the active cognitive

7. CONCLUSION

tasks that are registered in the entire 3-D brain volume while performing a typical fMRI experimental protocol that includes visuo-motor tasks.

It is very interesting to see that the real fMRI dataset ‘ds101’, which corresponds to a visuo-motor task, produces much higher estimated FD values than the corresponding FD values for the ‘ds105’, which is a much simpler visual recognition-only task. This means that, as expected, in the second task there is a much lower number of distinct activated brain areas, hence much fewer independent cognitive tasks involved, when no motor response is required by the experimental protocol. This does not mean that the total volume of brain activation is smaller but rather than fewer functionality components (‘sources’) are present *in parallel* when visual recognition is concerned, rather than when a proper motor response is required by the subject. This is inherently the casual link to ‘cpu cores’, where several processes are enabled to run simultaneously in a digital computer. ICA reconstruction plots show that when the human brain is concerned, this number is not defined as a strict threshold but rather in a continuous range; when a specific activation level is defined, a corresponding number of ‘brain cores’ can be evaluated. However, in real fMRI data, this range seems to be non-linear and such a number can be retrieved at the point beyond which adding more components has only marginal impact to the modeled brain signal (see Figures 7 and 8).

In short, it seems that normal brain functionality, such as in typical visual or visuo-motor tasks, involves only a limited number of independent processes that run in parallel. Some of them are related to this specific task, while others correspond to basic low-level functionality, e.g. respiration. Although it is difficult to correctly identify and explain all these components in strictly data-driven approaches (especially in BSS methods like ICA), the investigation of the number of major components, in combination with non-parametric dimensionality recovery methods such as dataset fractal analysis, can provide very useful hints for developing brain-like technologies and algorithms.

Current research endeavors like the Human Brain Project (HBP) by EU [18] and Brain Research through Advancing Innovative Neurotechnologies (BRAIN) by USA [47], as well as new innovative VLSI technologies like ‘TrueNorth’ project by IBM [37,44], require reliable evaluations of brain activity not only in the structural but also in the functional level. A typical voxel size of $3 \times 3 \times 3.5\text{--}5 \text{ mm}^3$ corresponds to roughly 2.5-4 million neurons of several thousands of synapse interconnections each, or $1/40000$ to $1/25000$ of the total brain volume, while the currently state-of-the-art ‘TrueNorth’ chip provides 1 million artificial neurons with only 256 synapses each. Hence, the level of true parallelism in human brain is a design aspect of paramount importance in future projects.

7 Conclusion

This study presents a purely data-driven approach to the estimation of the level of *parallelism* in human brain. Using fMRI as the main modality, the human brain activity was investigated through ICA for BSS, as well as dataset fractal

analysis for the estimation of the intrinsic (true) dimensionality of fMRI data. In some very abstract sense, this is not much different than trying to recover the (minimum) number of actual ‘cpu cores’ required to ‘run’ all the active cognitive tasks that are registered in the entire 3-D brain volume while performing a typical fMRI experimental protocol that includes visual-only or visuo-motor tasks.

Analysis of the non-smoothed variants of the real fMRI datasets (i.e., no information loss) proved that even when performing complex visuo-motor tasks, the number of independent brain processes are in the order of 50 to 60, while it becomes much lower when visual recognition tasks (no motor response) is concerned. This means that, in theory, an artificial equivalent of a brain-like cognitive structure may not require a massively parallel architecture at the level of single neurons, but rather a properly designed set of limited processes that run in parallel on a much lower scale. Hence, although current state-of-the-art VLSI technologies still include very limited features and processing power when compared to the real human brain, the assertion of employing actual parallelism level of much lower order can provide useful hints to future projects.

Acknowledgments The author wishes to thank professor Sergios Theodoridis, Yiannis Kopsinis and Anastassios Fytsilis, colleagues at the Dept. of Informatics & Telecommunications, National Kapodistrian Univ. of Athens (NKUA/UoA), for their collaboration in related projects and the useful discussions for works-in-progress in fMRI analysis and sparse modeling.

References

1. Vahid Abolghasemi, Saideh Ferdowsi, and Saeid Sanei. Blind separation of image sources via adaptive dictionary learning. *IEEE Transactions on Image Processing*, 21(6):2921–2930, June 2012.
2. Vahid Abolghasemi, Saideh Ferdowsi, and Saeid Sanei. Fast and incoherent dictionary learning algorithms with application to fMRI. *Signal, Image and Video Processing*, February 2013.
3. Trine Julie Abrahamsen and Lars Kai Hansen. Sparse non-linear denoising: Generalization performance and pattern reproducibility in functional MRI. *Pattern Recognition Letters*, 32(15):2080–2085, November 2011.
4. B. Abrahao and L. Barbosa. Characterizing datasets using fractal methods. *Dept. of Computer Science, Universidade Federal de Minas Gerais, Belo Horizonte, MG Brazil*, 2003.
5. M. Behroozi, M. R. Daliri, and H. Boyaci. Statistical analysis methods for the fmri data. *Basic and Clinical Neuroscience*, 2(4):67–74, 2011.
6. A. J. Bell and T.J. Sejnowski. An information maximisation approach to blind separation and blind deconvolution. *Neural Computation*, 7:1129–1159, 1995.
7. V. D. Calhoun, T. Adali, J. Hansen, L. K. and Larsen, and J. J. Pekar. Ica of functional mri data: An overview. In *Proc. Int. Symp. Indep. Comp. Analysis (ICA 2003)*.
8. V. D. Calhoun, T. Adali, G. D. Pearlson, and J. J. Pekar. Spatial and temporal independent component analysis of functional mri data containing a pair of task-related waveforms. *Human Brain Mapping*, 13(1):43–53, May 2001.

7. CONCLUSION

9. C. C. Chen, J. S. Daponte, and Fox M. D. Fractal feature analysis and classification in medical imaging. *IEEE Trans. Med. Im.*, 8(2):133–142, 1989.
10. Gang Chen, Ziad S. Saad, Jennifer C. Britton, Daniel S. Pine, and Robert W. Cox. Linear mixed-effects modeling approach to fMRI group analysis. *NeuroImage*, 73:176–190, June 2013.
11. M. K. Chung. Gaussian kernel smoothing. *Lecture notes*, pages 1–10, 2012.
12. M. K. Chung. *Statistical and Computational Methods in Brain Image Analysis*. CRC Press, USA, 2013.
13. N. Correa, T. Adali, Yi-Ou Li, and V.D. Calhoun. Comparison of blind source separation algorithms for fmri using a new matlab toolbox: Gift. In *Acoustics, Speech, and Signal Processing, 2005. Proceedings. (ICASSP '05). IEEE International Conference on*, volume 5, pages v/401–v/404 Vol. 5, March 2005.
14. K. P. Cosgrove, C. M. Mazure, and J. K. Staley. Evolving knowledge of sex differences in brain structure, function, and chemistry. *Biol Psychiat*, 62(8):847–855, 2007.
15. ARP (DoE-USA). Artificial retina project (arp) – <http://artificialretina.energy.gov/>.
16. J. L. Encarnacao, H.-O. Peitgen, G. Sakas, and G. (Eds.) Englert. *Fractal Geometry and Computer Graphics*. Springer-Verlag, Berlin, 1992.
17. Erik Barry Erhardt, Srinivas Rachakonda, Edward J. Bedrick, Elena A. Allen, TÁElay Adali, and Vince D. Calhoun. Comparison of multi-subject ica methods for analysis of fmri data. *Human Brain Mapping*, 32(12):2075–2095, 2011.
18. HBP (EU). The human brain project (hbp) – <http://www.humanbrainproject.eu/>.
19. H. Georgiou, M. Mavroforakis, N. Dimitropoulos, D. Cavouras, and S. Theodoridis. Multi-scaled morphological features for the characterization of mammographic masses using statistical classification schemes. *Artificial Intelligence in Medicine*, 41(1):39–59, 2007.
20. S. J. Hanson, T. Matsuka, and J. V. Haxby. Combinatorial codes in ventral temporal lobe for object recognition: Haxby (2001) revisited: is there a ‘face’ area? *Neuroimage*, 23(1):156–166, 2004.
21. F. J. Harris. On the use of windows for harmonic analysis with the discrete fourier transform. *Proc.IEEE.*, 66:66–67, 1978.
22. J. Haxby, M. Gobbini, M. Furey, A. Ishai, J. Schouten, and P. Pietrini.
23. J. V. Haxby, M. I. Gobbini, M. L. Furey, A. Ishai, J. L. Schouten, and P. Pietrini. Distributed and overlapping representations of faces and objects in ventral temporal cortex. *Science*, 293(5539):2425–2430, 2001.
24. A. Hyvärinen. Fast and robust fixed-point algorithms for independent component analysis. *Neural Networks*, 10:626–634, 1999.
25. A. Hyvarinen, J. Karhunen, and E. Oja. *Independent Component Analysis*. Wiley-Interscience, 2001.
26. A. Hyvärinen and E. Oja. A fast fixed-point algorithm for independent component analysis. *Neural Computation*, 9(7):1483–1492, 1997.
27. Andreas Jung. An introduction to a new data analysis tool: Independent component analysis. In *Proceedings of Workshop GK " Nonlinearity "-Regensburg*, 2001.
28. A. M. Kelly and Milham M. P. ds101: Nyu simon task – openfmri.org (dataset), 2011.
29. Yannis Kopsinis, Harris Georgiou, and Sergios Theodoridis. fmri unmixing via properly adjusted dictionary learning. In *22th European Signal Processing Conference (EUSIPCO 2014)*.
30. N. Lazar. *The Statistical Analysis of Functional MRI Data*. Springer, 2008.

31. K. Lee and J. C. Ye. A data-driven fmri analysis using k-svd sparse dictionary learning. *International Society of Magnetic Resonance in medicine (ISMRM)*, 2010.
32. Kangjoo Lee, Sungho Tak, and Jong Chul Ye. A data-driven sparse GLM for fMRI analysis using sparse dictionary learning with MDL criterion. *IEEE Transactions on Medical Imaging*, 30(5):1076–1089, May 2011.
33. Martin A. Lindquist. The statistical analysis of fMRI data. *Statistical Science*, 23(4):439–464, November 2008.
34. P. R. Massopust. *Fractal Functions, Fractal Surfaces and Wavelets*. Academic Press, San Diego, 1994.
35. M. Mavroforakis, H. Georgiou, N. Dimitropoulos, D. Cavouras, and S. Theodoridis. Significance analysis of qualitative mammographic features using linear classifiers, neural networks and support vector machines. *European Journal of Radiology*, 54:80–89, 2005.
36. M. Mavroforakis, H. Georgiou, N. Dimitropoulos, D. Cavouras, and S. Theodoridis. Mammographic masses characterization based on localized texture and dataset fractal analysis using linear, neural and support vector machine classifiers. *Artificial Intelligence in Medicine*, 37(2):145–162, 2006.
37. Paul A. Merolla, John V. Arthur, Rodrigo Alvarez-Icaza, Andrew S. Cassidy, Jun Sawada, Filipp Akopyan, Bryan L. Jackson, Nabil Imam, Chen Guo, Yutaka Nakamura, Bernard Brezzo, Ivan Vo, Steven K. Esser, Rathinakumar Appuswamy, Brian Taba, Arnon Amir, Myron D. Flickner, William P. Risk, Rajit Manohar, and Dharmendra S. Modha. A million spiking-neuron integrated circuit with a scalable communication network and interface. *Science*, 345(6197):668–673, 2014.
38. MLSP-Lab. Machine learning for signal processing laboratory – <http://mlsp.umbc.edu/>.
39. A. W. Moore and M. S. Lee. Efficient algorithm for minimizing cross validation error. In *Proceedings of the 11th. International Conference on Machine Learning (ML-94), 10-13 July 1994, New Brunswick, New Jersey*.
40. National Institute of Mental Health (NIMH) and National Institute of Neurological Disorders Stroke (NINDS). Neuroimaging informatics technology initiative (nifti) – <http://nifti.nimh.nih.gov/background>.
41. A. J. O’Toole, F. Jiang, H. Abdi, and J. V. Haxby. Partially distributed representations of objects and faces in ventral temporal cortex. *J Cogn Neurosci.*, 17(4):580–590, 2005.
42. A. Parent and M. B. Carpenter. *Carpenter’s Human Neuroanatomy*. Williams-Wilkins, 1995.
43. S. Pierre and J. F. Rivest. On the validity of fractal dimension measurements in image analysis. *J. Vis. Com. Im. Proc.*, 7(3):217–229, 1996.
44. A. Sebastian. Ibm cracks open a new era of computing with brain-like chip: 4096 cores, 1 million neurons, 5.4 billion transistors – <http://www.extremetech.com/extreme/187612-ibm-cracks-open-a-new-era-of-computing-with-brain-like-chip-4096-cores-1-million-neurons-5-4-billion-transistors>.
45. S. M. Smith. Overview of fmri analysis. *The British Journal of Radiology*, 77:S167–S175, 2004.
46. C. Jr. Traina, A. J. Traina, L. Wu, and C. Faloutsos. Fast feature selection using fractal dimension. In *XV Brazilian Database Symposium 2000, Joao Pessoa, PA Brazil*.
47. BRAIN (USA). Brain research through advancing innovative neurotechnologies (brain) – <http://www.braininitiative.nih.gov/>.